DOI: 10.1002/ejic.200901066

The Effect of Surface Area and Crystal Structure on the Catalytic Efficiency of Iron(III) Oxide Nanoparticles in Hydrogen Peroxide Decomposition

Cenek Gregor,[a,b] Martin Hermanek,[c] Dalibor Jancik,[a,c] Jiri Pechousek,[a,c] Jan Filip,[a,c] Jan Hrbac,[a,b] and Radek Zboril*[a,b,d]

Keywords: Solid-state reactions / Iron / Nanoparticles / Moessbauer spectroscopy / Heterogeneous catalysis

Iron(II) oxalate dihydrate has been used as a readily decomposable substance for the controlled synthesis of nanosized iron(III) oxides. The polymorphous composition, particle size and surface area of these iron oxide nanoparticles were controlled by varying the reaction temperature between 185 and 500 °C. As-prepared samples were characterized by XRD, low-temperature and in-field Mössbauer spectroscopy, BET surface area and the TEM technique. They were also tested as heterogeneous catalysts in hydrogen peroxide decomposition. At the selected temperatures, the formed nanomaterials did not contain any traces of amorphous phase, which is known to considerably reduce the catalytic efficiency of iron(III) oxide catalysts. As the thickness of the sample (≈ 2 mm) was above the critical value, a temporary temperature increase ("*exo* effect") was observed during all quasi-isothermal decompositions studied, irrespective of the reaction temperature. Increasing the reaction temperature resulted in a shift of the *exo* effect towards shorter times and an increased content of maghemite phase. The maghemite content decreases above 350 °C as a result of a thermally induced polymorphous transition into hematite. The catalytic data demonstrate that the crystal structure of iron(III) oxide (i.e. the relative contents of maghemite and hematite) does not influence the rate of hydrogen peroxide decomposition. However, the rate constant increases monotonously with increasing sample surface area (and decreasing thermolysis temperature), reaching a maximum of $27 \times 10^{-3}\ \mathrm{min}^{-1}(\mathrm{g/L})^{-1}$ for the sample with a surface area of $285\ \mathrm{m}^2\,\mathrm{g}^{-1}$. This rate constant is currently the highest reported value of all known iron oxide catalytic systems and is even slightly higher than that observed for the most efficient catalyst reported to date, which has a significantly larger surface area of $337\ \mathrm{m}^2\,\mathrm{g}^{-1}$. This surprisingly high catalytic activity at relatively low surface area can be ascribed to the absence of a amorphous phase in the samples prepared in this study. Taking into account these new findings, the contributions of the key factors highlighted above (surface area, particle size, crystal structure, crystallinity) to the overall activity of iron oxides for hydrogen peroxide decomposition are discussed.

Introduction

Iron oxides, in their various forms, are very important and interesting materials, therefore research into their properties is at the forefront of modern science. The structure, size, shape and morphology of iron oxide particles determine their properties and behaviour and lead to diverse applications within the fields of medicine,[1–6] industry and environmental protection. Among the numerous applications to exploit the specific properties of iron oxides, the production of inorganic pigments and magnetic storage media,[7–11] the development of gas sensors and electronic and optical devices, information storage, colour imaging, magnetocaloric refrigeration, bioprocessing and ferrofluid technology[12–19] can be highlighted. Iron oxides are also indispensable catalysts for many industrially important reactions[20–23] due to their environmental benefits. Significant attention has been paid over the last two decades to the degradation of organic pollutants in wastewaters and contaminated soils.[24–43] Iron oxides have been extensively tested as alternatives for soluble forms of $\mathrm{Fe^{II}}$ and $\mathrm{Fe^{III}}$, which are frequently used as homogeneous catalysts for hydrogen peroxide decomposition.[44–47] During this process, a highly reactive hydroxyl radical ($\mathrm{HO^{\cdot}}$) is formed which is able to oxidatively decompose even highly resistant (biotoxic) aromatic compounds. The kinetics of H_2O_2 decomposition is strongly influenced by catalyst type and, of course, by experimental conditions such as pH and hydrogen peroxide and catalyst concentration.[39,48,49] In the case of homogeneous catalysis, an acidic pH (typically 2–4) is required for efficient pollutant degradation. The major drawbacks for application of these homogeneous catalysts are the need for pH adjustment and separation of the ferric

---

[a] Nanomaterial Research Centre, Faculty of Science, Palacky University in Olomouc,
17, listopadu 1192/12, 77146 Olomouc, Czech Republic
[b] Department of Physical Chemistry, Faculty of Science, Palacky University in Olomouc,
17, listopadu 1192/12, 77146 Olomouc, Czech Republic
[c] Department of Experimental Physics, Faculty of Science, Palacky University in Olomouc,
17, listopadu 1192/12, 77146 Olomouc, Czech Republic
[d] Department of Physical Chemistry, Faculty of Science, Palacky University,
Svobody 26, 77146 Olomouc, Czech Republic
Fax: +42-0585634958
E-mail: zboril@prfnw.upol.cz

oxyhydroxide precipitates formed in the reaction mixtures. The processes that use iron(II) or iron(III) ions as catalysts are well known to be Fenton or Fenton-like reaction systems, respectively. The use of iron oxides as heterogeneous catalysts is possible over a wider pH range, including at neutral values, and physical sedimentation can be used to separate the catalyst after completion of the reaction.

It is well known that *surface area* is the main aspect influencing the reaction rate during heterogeneous catalysis, as exemplified by the detailed study of the catalytic efficiency of three iron(III) oxides with different chemical compositions (ferrihydrite, goethite and hematite) for hydrogen peroxide decomposition reported by Huang et al.[39]. The specific surface areas for ferrihydrite, goethite and hematite were reported to be 190, 40 and 9 $m^2 g^{-1}$, respectively. The rate constant obtained for ferrihydrite was two orders of magnitude higher than those for goethite and hematite, although the catalytic activity of all three oxides was nearly comparable when the rate constants were normalized to the surface area. This conclusion confirms the principal role of the surface area of the catalyst used and also indicates that catalytic efficiency is not dramatically affected by the *chemical composition* of iron(III) oxides.

In a previous paper we reported a new factor affecting the catalytic activity, namely the *crystallinity* of the iron(III) oxide, which can prevail over the surface area effect.[50] The key conclusion of this study was that the highest rate constant was not observed for the almost amorphous ferric oxide sample with the largest surface area (401 $m^2 g^{-1}$) but for the sample with a significantly lower surface area (337 $m^2 g^{-1}$) but with a much higher content of crystalline α-Fe_2O_3 phase. This study proved that the surface "quality" can play an important role in the catalytic efficiency of iron(III) oxide catalysts. Unfortunately, there are still no reports describing the possible catalytic effect of *particle structure* (i.e. hematite vs. maghemite) or *particle morphology* on hydrogen peroxide decomposition.

This scientific gap is due, among others, to the difficulty in controlling the main catalytic parameters (surface area, particle size and crystallinity, particle structure and morphology) in the framework of one synthetic procedure. The most frequent synthetic methods for producing iron(III) oxide nanoparticles include a precipitation approach, sonochemical syntheses, thermolysis of Fe-containing solutions, oxygen-hydrogen flame pyrolysis, electrochemical syntheses, sol-gel methods, vaporization-condensation processes, microemulsion techniques, diode sputter depositions and thermal decomposition of iron-containing materials in the solid state.[51] The thermally induced solid-state decomposition of appropriate Fe precursors is a powerful method that allows the particle structure, size, morphology, surface area and crystallinity of the iron oxide phase to be controlled by varying the reaction conditions (atmosphere, temperature, powder thickness) and precursor properties (composition, structure, particle size and morphology). One of the most commonly used precursors is ferrous oxalate dihydrate ($FeC_2O_4{\cdot}2H_2O$), which is a typical example of a readily decomposable substance. The course of ferrous oxalate thermolysis has been extensively studied in recent years,[52–59] although it is still difficult to reach an unambiguous conclusion from the published data. Differences in the published results arise due to the different experimental conditions applied, which substantially affect the final composition of the iron oxide product.[60,61]

Herein we demonstrate that the polymorphous composition and particle size of iron(III) oxides prepared by thermal treatment of iron(II) oxalate dihydrate can be controlled by varying the amount of precursor used (sample layer thickness) and the reaction temperature. Thus, a series of iron(II) oxalate dihydrate samples were heated at different reaction temperatures for a constant time (6 h) and the resulting nanomaterials identified as mixtures of hematite and maghemite by Mössbauer spectroscopy and X-ray powder diffraction (XRD). The specific surface areas of these materials were determined by BET analysis and the morphology of the samples was studied by transmission electron microscopy (TEM). The resulting iron(III) oxide products show remarkable differences in their catalytic efficiencies for hydrogen peroxide decomposition. Kinetic analyses of hydrogen peroxide decomposition were carried out for all samples prepared and data obtained are compared with our previous results.[50]

Results and Discussion

The Effect of Decomposition Temperature on the Crystal Structure and Particle Size of Iron(III) Oxide Nanomaterials

The thermolysis of iron oxalate at temperatures ranging from 185–500 °C yielded iron oxides with different particle sizes, surface area and phase composition. The particle

Table 1. Specific surface areas and particle sizes for samples A1–A18 prepared at different temperatures.

T_{calc}[a]	SSA[b]	PS[c]	T_{calc}[a]	SSA[b]	PS[c]	T_{calc}[a]	SSA[b]	PS[c]
185 °C, A_1	285	3–7	235 °C, A_7	160	–	295 °C, A_{13}	100	–
190 °C, A_2	259	–	245 °C, A_8	146	–	300 °C, A_{14}	93	20–30
195 °C, A_3	240	5–8	255 °C, A_9	141	10–15	350 °C, A_{15}	36	30–50
205 °C, A_4	220	–	265 °C, A_{10}	130	–	400 °C, A_{16}	27	50–100
215 °C, A_5	195	–	275 °C, A_{11}	122	–	450 °C, A_{17}	24	70–130
225 °C, A_6	177	8–12	285 °C, A_{12}	114	–	500 °C, A_{18}	14	100–200

[a] Reaction Temperature. [b] Specific surface area [$m^2 g^{-1}$]. [c] Particle size [nm].

sizes, as determind by TEM, and specific surface areas, as determined by the standard BET method, for the samples studied in this work are summarized in Table 1. The dependence of the samples' surface areas on the preparation temperature can be seen from Figure 1, which shows a gradual decrease in surface area with reaction temperature as a consequence of the different rates of particle growth resulting from the thermally induced crystallization.

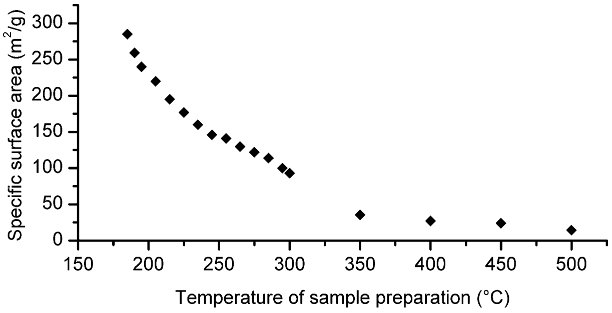

Figure 1. Dependence of the specific surface areas of catalysts on the reaction temperature.

The presence of maghemite and hematite in sample A1, which was prepared at the lowest temperature (185 °C), was confirmed. These nanoparticles have a globular shape with a size distribution in the range 3–7 nm, as can be seen from the TEM image (Figure 2, a). The diffraction peaks corresponding to hematite and maghemite can clearly be seen in the XRD pattern for this sample (Figure 3, a), although they are still very broad due to the very small size of the emerging nanograins. The room-temperature Mössbauer spectrum contains only the expected superparamagnetic doublet (Figure 4, a), thereby reflecting the ultra-small size of these particles. The hyperfine parameters of this doublet (Table 2) are similar to those reported previously for Fe_2O_3 nanoparticles prepared by other synthetic routes.[62–65] The non-Lorentzian shape of the doublet is caused by the distribution of the quadrupole splitting and reflects the distorted symmetry of the charge distribution around the Fe^{3+} cores.

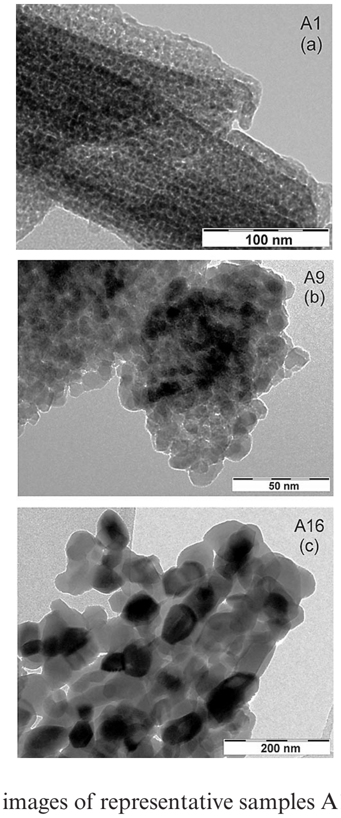

Figure 2. TEM images of representative samples A1 (a), A9 (b) and A16 (c) prepared at 185, 255 and 400 °C, respectively.

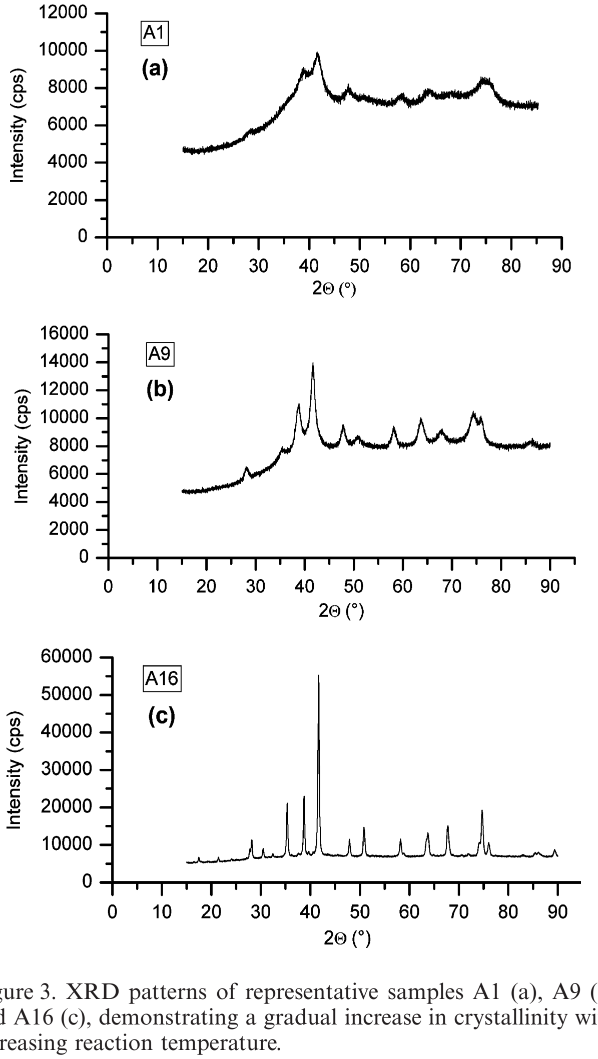

Figure 3. XRD patterns of representative samples A1 (a), A9 (b) and A16 (c), demonstrating a gradual increase in crystallinity with increasing reaction temperature.

The Mössbauer spectrum at 5 K in an external magnetic field of 5 T was measured to determine the phase composition of sample A1 (Figure 5, a). This spectrum can be fitted by three sextets differing primarily in their effective magnetic fields, quadrupole shifts and line intensities. The first sextet, which has a hyperfine magnetic field of 50.9 T, belongs to hematite and the next two sextets, with hyperfine magnetic fields of 54.7 and 47.4 T, respectively, are assigned

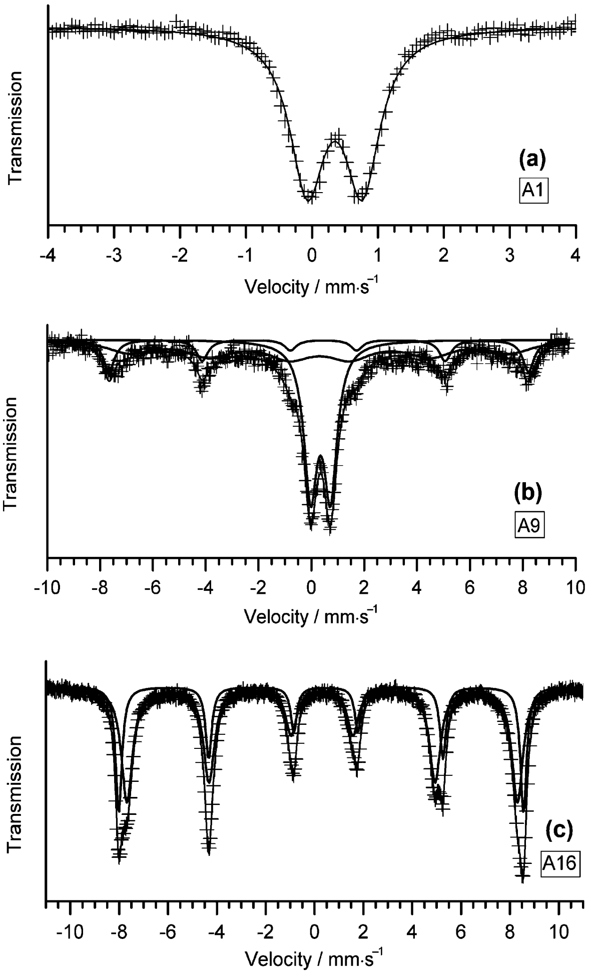

Figure 4. Room-temperature Mössbauer spectra of representative samples A1 (a), A9 (b) and A16 (c) prepared by isothermal decomposition of $FeC_2O_4{\cdot}2H_2O$ at 185, 255 and 400 °C, respectively.

to the maghemite phase. In the case of well-crystalline hematite, the second and the fifth spectral lines are distinctly enhanced (ideally 3:4:1:1:4:3) and those of maghemite attenuated (ideally 3:0:1:1:0:3). These differences arise from the antiferromagnetic and ferrimagnetic behaviour of hematite and maghemite, respectively. The particles in sample A1 are very small and/or preferentially oriented, therefore the second and fifth spectral lines of hematite are less intense in the corresponding in-field sub-spectrum, whereas the second and fifth spectral lines in the in-field sub-spectra of maghemite are clearly observed. These non-ideal intensity ratios are caused by so-called spin frustration, which induces disorder of the atomic moments' directions.[51,66] The sextet corresponding to hematite exhibits a negative quadrupole shift (–0.13 mm/s) typical for weakly ferromagnetic hematite above the Morin temperature (normally 265 K). It should be noted at this point that hematite nanoparticles smaller than 20 nm commonly exhibit such a massive reduction of the Morin transition temperature.[51] The other two sextets have quadrupole shifts close to zero and are ascribed to maghemite. The maghemite sub-spectra area ratio (5/6 here, ideally 3/5) reflects the tetrahedral and octahedral Fe^{3+} positions in the maghemite structure, therefore this deviation suggests a highly vacant structure.

The room-temperature Mössbauer spectra of the samples prepared at reaction temperatures of 195 °C or higher contain sextets in addition to the expected superparamagnetic doublet (Figure 4). The gradual increase in the area of these sextets observed with increasing sample-preparation temperature is accompanied by a corresponding decrease in the relative content of the central superparamagnetic component. These changes in the room-temperature spectra are caused by the gradual growth of hematite and maghemite particles. Growth of the crystalline phase is also obvious from the XRD data (Figure 3) and TEM analysis (Figure 2). Thus, the XRD pattern of sample A9 shows much sharper diffraction peaks belonging to hematite and maghemite (Figure 3, b) than the XRD pattern of sample A1 (Figure 3, a). Furthermore, the TEM image (Figure 2, b) shows nanoparticles with a size distribution of 10–15 nm. It should be noted that the spectral area of the hematite sextet decreases at the expanse of maghemite sextets. A gradual increase in maghemite content is found in those samples prepared at temperatures between 185 and 350 °C, as can be seen from their Mössbauer spectra (see Table 2). After reaching a maximum of 84 %, the maghemite content gradually decreases until the sample prepared at 500 °C contains only hematite. The dependence of the hematite and maghemite ratios on the preparation temperature is shown in Figure 6.

The room-temperature Mössbauer spectrum of sample A16 (400 °C) is composed of sextets only (Figure 4, c). The fact that the superparamagnetic doublet is no longer observed indicates that the crystalline phases are well developed. The XRD peaks for this sample are distinct and sharp (Figure 3, c) and the TEM image shows particles ranging from 50 to 100 nm in size (Figure 2, c).

The highest sample-preparation temperature used was 500 °C, and the resulting product was unambiguously identified as single-phase hematite by both XRD and Mössbauer techniques.

The data presented in this work indicate that both the decomposition temperature and the sample thickness have a significant influence on the phase composition of the resulting product. Thus, if the thickness of the sample layer is above a minimum thickness, a steep time-dependent increase in the temperature (*exo* effect) is observed during the thermal decomposition.[61] In the case of ferrous oxalate dihydrate, the *exo* effect leads to the formation of maghemite, whereas below the critical thickness hematite is the only polymorph produced at the same reaction temperature. In the case of sample A1, the *exo* effect arises about 43 min after inserting the crucible containing the precursor into the furnace (Figure 7). In light of our previous results,[61] we suppose that, upon thermolysis, amorphous Fe_2O_3 and hematite form gradually in the upper layer of the sample where oxygen is readily accessible, whereas during the *exo* effect, the remaining FeC_2O_4 rapidly decomposes to form

Table 2. Mössbauer parameters of iron(III) oxide samples prepared by thermal decomposition of $FeC_2O_4{\cdot}2H_2O$ at different temperatures.

Sample	T_{calc}[a]	T_{meas}[b]	δ [mm s^{-1}][c]	ΔE_Q [mm s^{-1}][d]	ε_Q [mm s^{-1}][e]	B [T][f]	RA [%][g]	Site assignment
A1	185 °C	r.t.	0.35	0.83			100	SP Fe_2O_3
		5 K/5 T	0.49		–0.13	50.9*	50	α-Fe_2O_3
			0.44		0.04	54.7*	23	γ-Fe_2O_3
			0.41		0.03	47.4*	27	γ-Fe_2O_3
A2	255 °C	r.t.	0.35	0.75			42	SP Fe_2O_3
			0.37		–0.19	49.3	16	α-Fe_2O_3
			0.32		0	44.8	42	γ-Fe_2O_3
		5 K/5 T	0.48		–0.09	50.7*	32	α-Fe_2O_3
			0.44		–0.04	53.5*	24	γ-Fe_2O_3
			0.46		–0.02	47.6*	44	γ-Fe_2O_3
A14	300 °C	r.t.	0.31	0.77			20	SP Fe_2O_3
			0.35		–0.19	50.5	16	α-Fe_2O_3
			0.31		–0.06	48.4	21	γ-Fe_2O_3
			0.33		–0.06	42.8	43	γ-Fe_2O_3
		5 K/5 T	0.48		–0.09	52.3*	23	α-Fe_2O_3
			0.41		–0.02	54.4*	23	γ-Fe_2O_3
			0.46		–0.01	48.6*	54	γ-Fe_2O_3
A15	350 °C	r.t.	0.37		–0.18	51.1	17	α-Fe_2O_3
			0.31		–0.01	49.5	72	γ-Fe_2O_3
			0.31		0	42.8	11	γ-Fe_2O_3
		5 K/5 T	0.49		0.1	54*	16	α-Fe_2O_3
			0.33		–0.04	54.3*	31	γ-Fe_2O_3
			0.48		–0.04	48.4*	53	γ-Fe_2O_3
A16	400 °C	r.t.	0.37		–0.19	51.5	34	α-Fe_2O_3
			0.31		0.01	49.7	66	γ-Fe_2O_3
		5 K/5 T	0.49		0.23	53.5*	33	α-Fe_2O_3
			0.33		–0.04	54.2*	26	γ-Fe_2O_3
			0.49		–0.04	48.4*	41	γ-Fe_2O_3
A17	450 °C	r.t.	0.38		–0.21	51.5	87	α-Fe_2O_3
			0.32		0.01	49.8	13	γ-Fe_2O_3
A18	500 °C	r.t.	0.35		–0.2	51.6	100	α-Fe_2O_3
		5 K/5 T	0.49		0.21	53.4	100	α-Fe_2O_3

[a] Reaction temperature. [b] Temperature at which the spectrum was recorded. [c] Isomer shift (with respect to metallic iron ±0.01). [d] Quadrupole splitting (±0.01). [e] Quadrupole shift (±0.01). [f] Hyperfine magnetic field (±0.5). [g] Relative spectrum area (±1). * These values represent an effective magnetic field, which is a vector sum of the external and hyperfine magnetic fields.

a maghemite phase in the bottom layer due to its oxygen deficiency. Once the *exo* effect is complete, the crystalline maghemite and hematite particles grow slowly for the remaining time. Thermolysis of sample A1 led to a product containing 50% maghemite and 50% hematite, as determined from the in-field Mössbauer spectra (Figure 6). The time-dependence of the sample temperatures (Figure 7) unambiguously shows that the *exo* effect occurs earlier as the reaction temperature increases. Shortening of the interval between onset of thermolysis and appearance of the *exo* effect markedly affects the amount of maghemite in the final product such that if the *exo* effect occurs almost immediately after onset of the decomposition process, most of the precursor is transformed into maghemite. Hence, the maximum amount of γ-Fe_2O_3 (84%) was found in the sample prepared at a reaction temperature of 350 °C (A15), where the *exo* effect emerged as early as after 5 min. The *exo* effects occur even earlier in the case of samples A16–A18 (400, 450 and 500 °C, respectively), although these higher temperatures induce the rapid structural transition of maghemite into hematite. Moreover, these samples are characterized by a larger interparticle space, thus allowing oxygen to penetrate further into the samples and resulting in a further decrease in the maghemite content of the products (Figure 6). Changes in the interparticle spaces can be seen by the BJH distributions for samples A1 (185 °C) and A16 (400 °C) shown in Figure 8. It is apparent from the distribution curves that sample A1 is characterised by interparticle spaces of around 3 nm arising from ultra-small nanoparticles, whereas this maximum is suppressed for sample A16. The larger interparticle spaces in sample A16 are confirmed by the occurrence of a different maximum at around 30 nm. These differences between the BJH curves are in accordance with the particle-growth data (Table 1 and Figure 2).

The data presented above show that, in agreement with our previous findings,[61] the combined influence of temperature and sample thickness has a decisive impact on the resulting amount of individual iron(III) oxide polymorphs formed during thermal decomposition of ferrous oxalate, which could explain the discrepancies found in the literature concerning the identified reaction products.

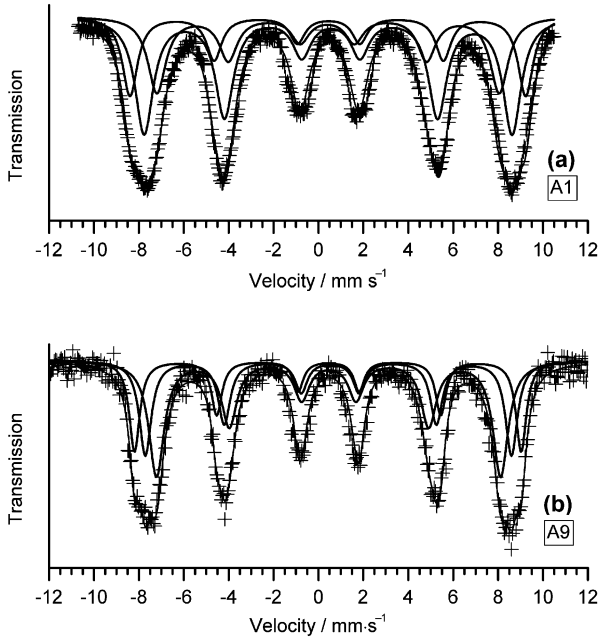

Figure 5. Mössbauer spectra of representative samples A1 (a) and A9 (b) taken at 5 K in an external magnetic field of 5 T applied parallel to the γ-ray propagation.

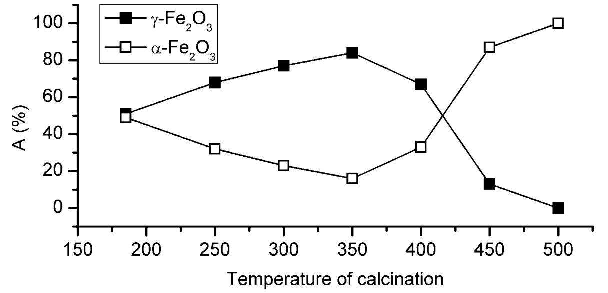

Figure 6. Maghemite and hematite contents as determined from the in-field Mössbauer spectroscopy data for samples prepared at different temperatures.

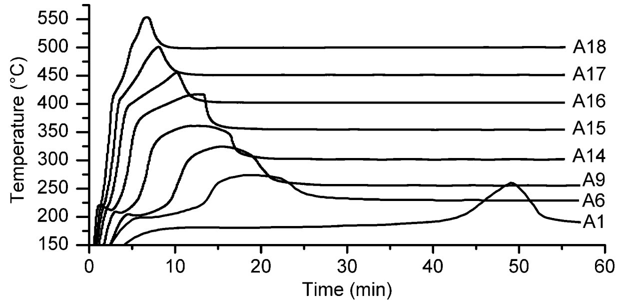

Figure 7. Time dependence of the temperature during thermal treatment of iron(II) oxalate dihydrate at different reaction temperatures.

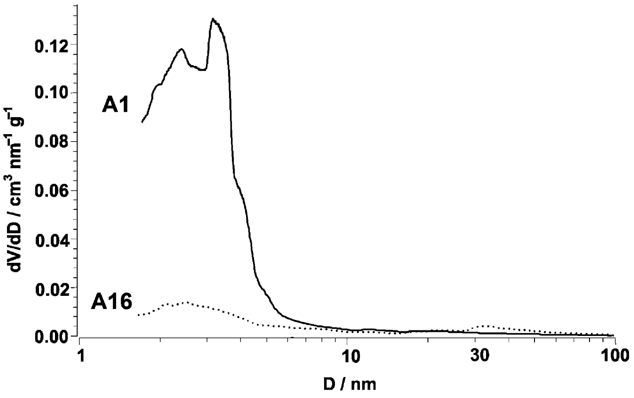

Figure 8. BJH distribution of interparticle spaces, as determined from adsorption/desorption isotherms.

The Catalytic Efficiency of Iron(III) Oxide Nanomaterials in Hydrogen Peroxide Decomposition

The rate constants of hydrogen peroxide decomposition over the prepared iron oxide catalysts were determined for all samples (A1–A18). The dependence of the rate constants on surface area is shown in Figure 9, where the rate constants obtained from our previous research[50] are included for comparison. The set of experimental points determined in this work is labelled as MH (Maghemite-Hematite), whereas the points determined in our previous study are labelled as AH (Amorphous-Hematite). The results of our previous study can be summarised as follows:[50] the catalyst (ferric oxide) containing a crystalline phase (α-Fe_2O_3) exhibited a markedly higher catalytic efficiency than amorphous iron(III) oxide despite having a significantly lower specific surface area (337 vs. 401 $m^2 g^{-1}$). Due to the different crystallinity of the samples, the obtained rate constants exhibited a non-monotonous dependence on the surface area of the iron oxide samples.

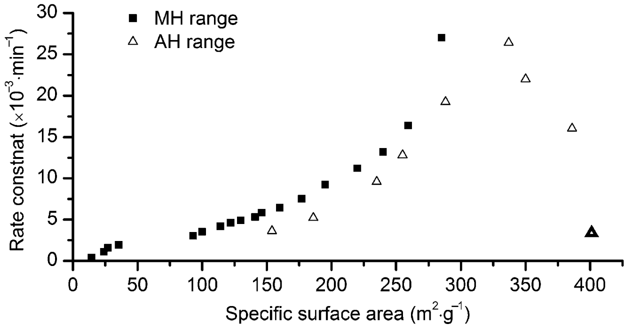

Figure 9. Dependence of the rate constant on the specific surface area of the synthesized Fe_2O_3 catalysts.

The MH series contains samples prepared by varying the reaction temperatures (185–500 °C) at constant reaction time (6 h), whereas the AH series contains samples prepared by varying the reaction time (6–100 h) at constant temperature (175 °C). The maghemite-to-hematite phase composition of the samples in the MH series depends on the reaction temperature. Furthermore, it should be noted that an additional decrease in temperature towards the minimum decomposition temperature of ferrous oxalate (175 °C), which is assumed to be the next step in the temperature-dependence series, leads to the formation of a mixture of hematite and amorphous iron(III) oxide, in other words to the first point in the AH series. Thus, even a slightly higher decomposition temperature (185 vs. 175 °C) can result in a major difference in the phase composition of the reaction products (MH vs. AH) and, consequently, in a dramatic difference in the catalytic efficiency of iron(III) oxide nanoparticles (27×10^{-3} vs. 3×10^{-3} $\mathrm{min^{-1}\,[g/L]^{-1}}$). This is the key conclusion derived from Figure 9 and also from the study as a whole.

The highest catalytic efficiency for the MH range therefore belongs to sample A1, which has a surface area of 285 $\mathrm{m^2\,g^{-1}}$. The rate constants determined for the other samples decrease gradually with their surface area. Taking into account the varying maghemite and hematite content in the samples prepared at different temperatures (see Figure 6), the observed monotonous dependence of the rate constant in the MH series illustrates that the crystal structure type of the iron(III) oxide catalyst (maghemite vs. hematite) does not affect the catalytic efficiency. Indeed, a comparison of the two plots demonstrates that the most efficient catalyst in the MH series has a significantly lower surface area (285 $\mathrm{m^2\,g^{-1}}$) than the most efficient sample from the AH range (337 $\mathrm{m^2\,g^{-1}}$). This is evidently due to the absence of an amorphous phase and thus a higher crystallinity for the sample from the MH series. Furthermore, the best catalyst from the MH series has the highest rate constant (27×10^{-3} $\mathrm{min^{-1}\,[g/L]^{-1}}$) of all iron oxide based catalysts reported in the literature to date.

Conclusions

We have provided an insight into the influence of the reaction temperature on the thermolysis of iron(II) oxalate and the polymorphous composition of the resulting iron(III) oxide nanoparticles as well as their size, surface area and catalytic efficiency in hydrogen peroxide decomposition. At an appropriate sample thickness above the critical thickness, we have been able to control the surface area of the samples as well as the content of their crystalline maghemite and hematite phases by varying the reaction temperature. The increasing maghemite content between 185 and 350 °C is explained by the earlier appearance of the *exo* effect. Hematite prevails in samples prepared above 400 °C due to the combined effects of increased sample porosity and thermally induced polymorphous transition of maghemite.

The key conclusion of this study is that the catalytic efficiency of the iron(III) oxides prepared herein in the decomposition of hydrogen peroxide is not dependent on their phase composition (molar ratio of hematite/maghemite). Indeed, as these nanomaterials were prepared by heating the precursor in conditions above the critical thickness, we were able to completely inhibit the formation of an amorphous iron(III) oxide phase, therefore the sample prepared at the lowest temperature studied (185 °C) exhibited a higher catalytic efficiency at a considerably lower surface area than the catalyst previously reported to be most efficient of all the iron oxide based systems studied previously.[50]

Experimental Section

Catalyst Synthesis: Iron(II) oxalate dihydrate ($\mathrm{FeC_2O_4{\cdot}2H_2O}$; Sigma–Aldrich) was used as a precursor for the solid-state synthesis of the iron(III) oxide nanomaterials described herein. The precursor was finely homogenized in an agate mortar before thermal treatment, then 1 g of this powdered precursor was spread in a thin layer (ca. 2 mm thick) on the bottom of a crucible and heated in air. Thermal decomposition of iron(II) oxalate dihydrate was performed at different temperatures (185–500 °C) for a constant reaction time (6 h). The samples are denoted as A1–A18.

Catalyst Characterization: TEM images were recorded with a JEOL JEM 2010 microscope operating at 200 kV ($\mathrm{LaB_6}$ cathode). The images were collected with a KeenView CCD camera with a resolution of 1392 × 1040 pixels using the ITEM software package. Sample material was disintegrated in ethanol solution by ultrasound, then the suspension was placed on a copper grid coated with holey carbon. The ethanol was then removed by evaporation at ambient temperature.

The transmission ^{57}Fe Mössbauer spectra (512 channels) were collected using a Mössbauer spectrometer in constant acceleration mode with a ^{57}Co(Rh) source. The basic measurements were carried out at room temperature. In-field Mössbauer spectra were recorded at 5 K in an external magnetic field of 5 T, applied parallel to the propagation of gamma rays, using a cryomagnetic Oxford Instruments system. The isomer shift values were referenced to α-Fe at room temperature.

X-ray powder diffraction experiments were performed with a PANalytical X'Pert PRO instrument (Co-K_α radiation) equipped with an X′Celerator detector and programmable divergence and diffracted beam anti-scatter slits. Samples were placed on zero-background Si slides, gently pressed in order to obtain a sample thickness of about 0.5 mm and scanned in the 2θ range 15–90° in steps of 0.017°.

Surface areas were determined by nitrogen adsorption at 77.4 K using the static volumetric technique on a Sorptomatic 1990 (Thermo Finnigan) instrument. All samples were degassed at 25 °C for at least 20 h prior to the measurements, although outgassing pressures lower than 0.1 Pa were commonly reached after 2–4 h. The adsorption-desorption isotherms were measured up to saturation pressure of nitrogen. The specific surface areas were determined by the multipoint BET3 method in the 0.0–0.5 relative pressurs range. Data analysis was performed with the ADP 4.0 (CE Instruments) software package.

Kinetic Measurements of Catalytic Decomposition of Hydrogen Peroxide: A flask containing a mixture of hydrogen peroxide (c_0 = 0.02 M) and the appropriate catalyst (1 $\mathrm{g\,L^{-1}}$; $\mathrm{H_2O_2/Fe_2O_3}$ molar ratio: 3.2) was shaken during the reaction to provide sufficient dispersion of the catalyst particles. The pH of the reaction mixture was not adjusted with buffer solution to avoid reaction of $\mathrm{HO^{\cdot}}$ radicals with the buffer solution. The pH varied from 6.3 to 6.5, as expected for a reaction in distilled water under standard atmosphere conditions. Samples of the solution were removed at various time points, filtered and the hydrogen peroxide concentration determined by titration with permanganate. Decomposition of hydrogen peroxide in the presence of iron oxide based catalysts follows first-order kinetics ($–d[H_2O_2]/dt = k_{obs}[H_2O_2]$), therefore $\ln([H_2O_2]/[H_2O_2]_0) = –k_{obs}t$, where k_{obs} is the observed first-order rate constant and $[H_2O_2]$ and $[H_2O_2]_0$ are the concentrations of hydrogen peroxide in the solution at any time t and at time zero, respectively.[37] This model was used to fit the collected kinetic data. The observed half-life for the least and the most efficient catalysts were 1691 and 25.7 min, respectively. As predicted, the kinetics of catalytic hydrogen peroxide decomposition obeyed first-order kinetics, as confirmed by a statistical analysis of the kinetic curves (R_2 ranged from 0.9988 to 0.9997).

Acknowledgments

This work was supported financially by projects from the Ministry of Education of the Czech Republic (1M6198959201 and MSM6198959218) and the ASCR (KAN115600801).

---

[1] Q. A. Pankhurst, J. Connolly, S. K. Jones, J. Dobson, *J. Phys. D: Appl. Phys.* **2003**, *36*, R167–R181.

[2] P. Tartaj, M. P. Morales, S. Veintemillas-Verdauger, T. Gonzalez-Carreño, C. J. Serna, *J. Phys. D: Appl. Phys.* **2003**, *36*, R182–R197.

[3] E. K. Ruuge, A. N. Rusetski, *J. Magn. Magn. Mater.* **1993**, *122*, 335–339.

[4] A. S. Lübbe, C. Alexiou, C. Bergemann, *J. Surg. Res.* **2001**, *95*, 200–206.

[5] R. Hiergeist, W. Andrä, N. Buske, R. Hergt, I. Hilger, U. Richter, W. Kaiser, *J. Magn. Magn. Mater.* **1999**, *201*, 420–422.

[6] E. H. Kim, Y. Ahn, H. S. Lee, *J. Alloys Compd.* **2007**, *434*, 633–636.

[7] G. Montes-Hernandez, J. Pironon, F. Villireas, *J. Colloid Interface Sci.* **2006**, *303*, 472–476.

[8] J. Bohacek, J. Subrt, T. Hanslik, *J. Mater. Sci.* **1993**, *28*, 2827–2832.

[9] S. K. Lim, K. J. Chung, Y. H. Kim, C. K. Kim, C. S. Yoon, *J. Colloid Interface Sci.* **2004**, *273*, 517–522.

[10] Q. A. Pankhurst, R. J. Pollard, *J. Phys. Condens. Matter* **1993**, *5*, 8487–8508.

[11] G. Bate, *J. Magn. Magn. Mater.* **1991**, *100*, 413–424.

[12] W. S. Choi, H. Y. Koo, Z. Zhongbin, Y. D. Li, D. Y. Kim, *Adv. Funct. Mater.* **2007**, *17*, 1743–1749.

[13] M. Z. Zayat, F. del Monte, M. P. Morales, G. Rosa, H. Guerrero, C. J. Serna, D. Levy, *Adv. Mater.* **2003**, *15*, 1809–1812.

[14] R. D. McMichael, R. D. Shull, L. J. Swartzendruber, L. H. Bennett, *J. Magn. Magn. Mater.* **1992**, *111*, 29–33.

[15] L. Günter, *Phys. World* **1990**, *3*, 28–34.

[16] G. Shön, U. Simon, *Colloid Polym. Sci.* **1995**, *273*, 101–117.

[17] L. Nixon, C. A. Koval, R. D. Noble, *Chem. Mater.* **1992**, *4*, 117–121.

[18] H. E. Horng, C. Y. Hong, S. Y. Yang, H. C. Yang, *J. Phys. Chem. Solids* **2001**, *62*, 1749–1764.

[19] K. Raj, B. Moskowicz, R. Casciari, *J. Magn. Magn. Mater.* **1995**, *149*, 174–180.

[20] N. Mimura, I. Takahara, M. Saito, T. Hattori, K. Ohkuma, M. Ando, *Catal. Today* **1998**, *45*, 61–64.

[21] L. G. Xu, S. Bao, R. J. O′Brien, D. J. Houpt, B. H. Davis, *Fuel Sci. Technol. Int.* **1994**, *12*, 1323–1353.

[22] A. M. van der Kraan, *Hyperfine Interact.* **1998**, *111*, 23–34.

[23] X. Wang, A. Wang, N. Li, X. Wang, Z. Liu, T. Zhang, *Ind. Eng. Chem. Res.* **2006**, *45*, 4582–4588.

[24] F. Martínez, G. Calleja, J. A. Melero, R. Molina, *Appl. Catal., B* **2005**, *60*, 181–190.

[25] G. Calleja, J. A. Melero, F. Martinez, R. Molina, *Water Res.* **2005**, *39*, 1741–1750.

[26] G. Ovejero, J. L. Sotelo, F. Martínez, J. A. Melero, L. Gordo, *Ind. Eng. Chem. Res.* **2001**, *40*, 3921–3928.

[27] G. Centi, S. Perathoner, T. Torre, M. G. Verduna, *Catal. Today* **2000**, *55*, 61–69.

[28] J. Barrault, M. Abdellaoui, C. Bouchoule, A. Majesté, J. M. Tatibouët, A. Louloudi, N. Papayannakos, N. H. Gangas, *Appl. Catal., B* **2000**, *27*, 225–230.

[29] E. Guélou, J. Barrault, J. Fournier, J. M. Tatibouët, *Appl. Catal., B* **2003**, *44*, 1–8.

[30] A. J. Khan, R. J. Watts, *Water Air Soil Pollut.* **1996**, *88*, 247–260.

[31] R. J. Watts, A. L. Teel, *J. Environ. Eng.* **2005**, *131*, 612–622.

[32] S. H. Kong, R. J. Watts, J. H. Choi, *Chemosphere* **1998**, *37*, 1473–1482.

[33] R. J. Watts, M. D. Udell, R. M. Monsen, *Water Environ. Res.* **1993**, *65*, 839–844.

[34] B. W. Tyre, R. J. Watts, G. C. Miller, *J. Environ. Qual.* **1991**, *20*, 832–838.

[35] R. L. Valentine, H. C. A. Wang, *J. Environ. Eng.* **1998**, *124*, 31–38.

[36] W. P. Kwan, B. M. Voelker, *Environ. Sci. Technol.* **2002**, *36*, 1467–1476.

[37] M. D. Gurol, S. S. Lin, *J. Adv. Oxid. Technol.* **2002**, *5*, 147–154.

[38] A. Cuzzola, M. Bernini, P. Salvadori, *Appl. Catal., B* **2002**, *36*, 231–237.

[39] H. H. Huang, M. C. Lu, J. N. Chen, *Water Res.* **2001**, *35*, 2291–2299.

[40] M. C. Lu, *Chemosphere* **2000**, *40*, 125–130.

[41] S. S. Lin, M. D. Gurol, *Environ. Sci. Technol.* **1998**, *32*, 1417–1423.

[42] S. S. Lin, M. D. Gurol, *Water Sci. Technol.* **1996**, *34*, 57–64.

[43] N. Al-Hayek, M. Doré, *Water Res.* **1990**, *24*, 973–982.

[44] M. Barbeni, C. Minero, E. Pelizzetti, E. Borgarello, N. Serpone, *Chemosphere* **1987**, *16*, 2225–2237.

[45] R. J. Watts, P. C. Stanton, *Water Res.* **1999**, *33*, 1405–1414.

[46] V. S. Millioli, D. D. C. Freire, M. C. Cammarota, *J. Hazard. Mater.* **2003**, *103*, 79–91.

[47] A. L. Teel, C. R. Warberg, D. A. Atkinson, R. J. Watts, *Water Res.* **2001**, *35*, 977–984.

[48] S. Chou, C. Huang, *Appl. Catal., A* **1999**, *185*, 237–245.

[49] E. Neyens, J. Baeyens, *J. Hazard. Mater.* **2003**, *98*, 33–50.

[50] M. Hermanek, R. Zboril, I. Medrik, J. Pechousek, C. Gregor, *J. Am. Chem. Soc.* **2007**, *129*, 10929–10936.

[51] R. Zboril, M. Mashlan, D. Petridis, *Chem. Mater.* **2002**, *14*, 969–982.

[52] V. Rao, A. L. Shashimohan, A. B. Biswas, *J. Mater. Sci.* **1974**, *9*, 430–433.

[53] K. S. Rane, A. K. Nikumbh, A. J. Mukhedkar, *J. Mater. Sci.* **1981**, *16*, 2387–2397.

[54] A. S. Brar, K. S. Khabre, *Indian J. Chem., Sect. A* **1982**, *21*, 920–921.

[55] B. Boyanov, D. Khadzhiev, V. Vasilev, *Thermochim. Acta* **1985**, *93*, 89–92.

[56] V. Borker, K. S. Rane, V. N. Kamat Dalal, *J. Mater. Sci. -. Mater. Electron* **1993**, *4*, 241–248.

[57] V. Chhabra, M. Lal, A. N. Maitra, P. Ayyub, *Colloid Polym. Sci.* **1995**, *273*, 939–946.

[58] N. N. Mallikarjuna, B. Govindaraj, A. Lagashetty, A. Venkataraman, *J. Therm. Anal. Calorim.* **2003**, *71*, 915–925.

[59] R. Zboril, L. Machala, M. Mashlan, M. Hermanek, M. Miglierini, A. Fojtik, *Phys. Status Solidi C* **2004**, *1*, 3583–3588.

[60] M. Hermanek, R. Zboril, M. Mashlan, L. Machala, O. Schneeweiss, *J. Mater. Chem.* **2006**, *16*, 1273–1280.

[61] M. Hermanek, R. Zboril, *Chem. Mater.* **2008**, *20*, 5284–5295.

[62] L. Machala, R. Zboril, A. Gedanken, *J. Phys. Chem. B* **2007**, *111*, 4003–4018.

[63] G. Ennas, A. Musinu, G. Piccaluga, D. Zedda, D. Gatteschi, C. Sangregorio, J. L. Stanger, G. Concas, G. Spano, *Chem. Mater.* **1998**, *10*, 495–502.
[64] T. Prozorov, R. Prozorov, Y. Koltypin, I. Felner, A. Gedanken, *J. Phys. Chem. B* **1998**, *102*, 10165–10168.
[65] X. N. Xu, Y. Wolfus, A. Shaulov, Y. Yeshurun, I. Felner, I. Nowik, Y. Koltypin, A. Gedankden, *J. Appl. Phys.* **2002**, *91*, 4611–4616.
[66] J. Tucek, R. Zboril, D. Petridis, *J. Nanosci. Nanotechnol.* **2006**, *6*, 926–947.

Received: November 3, 2009